Paraxial reconstruction

Conversion of homogeneous lens forms to continuous gradient-index media

Boyd, Andrew; Bociort, Florian

DOI
10.1364/AO.532452

Publication date
2024

Document Version
Final published version

Published in
Applied Optics

applied optics

Paraxial reconstruction: conversion of homogeneous lens forms to continuous gradient-index media

ANDREW BOYD[1,*] AND FLORIAN BOCIORT[2]

[1]Optical Systems, Excelitas Technologies, Glascoed Road, St Asaph, LL17 0LL Wales, United Kingdom
[2]Optics Research Group, Department of Imaging Physics, TU Delft, Lorentzweg 1, 2628 CJ Delft, The Netherlands
*andrew.boyd@excelitas.com

Received 10 June 2024; revised 11 August 2024; accepted 13 August 2024; posted 13 August 2024; published 17 September 2024

We present a technique for the optical design of generalized-distribution GRIN lenses. Multi-element homogeneous lens designs are reconstructed as single GRIN media via smoothing of the homogeneous lens paraxial ray paths. These continuous optical systems successfully replicate the first-order properties of their homogeneous parent lens systems and serve as starting points for further optimization. When the technique is applied at several wavelengths, the chromatic aberration correction of the homogeneous parent lens is also converted. The paraxial reconstruction, finite-ray optimization, and evaluation of several lens designs are demonstrated.

https://doi.org/10.1364/AO.532452

1. INTRODUCTION

In recent years there has been a resurgence of interest in gradient-index (GRIN) optics. This is significantly due to the development of a range of new manufacture methods that address ongoing requirements to reduce size, weight, power consumption, and cost (referred to as SWAP-C) of optical systems. In particular, additive manufacture [1,2] and targeted modification techniques [3] enable the manufacture of GRIN lenses of arbitrary refractive index distribution. Such manufacture approaches allow multiple lens components (and potentially entire optical assemblies) to consist of as few as one GRIN lens, where the optical work performed by several discrete optical surfaces is instead performed by a continuous GRIN medium. We refer to such optics as *continuous optical systems*, abbreviated to COS herein. The combination of the degrees of freedom for aberration correction provided by GRIN optics, with scalable yet flexible additive manufacture, promises a new route to provide improved SWAP-C optics. There is therefore a strong motivation to develop optical design tools for COS.

A significant decision in the optical design process is the selection of a starting solution that, if chosen well, leads to a high performing and cost-effective final design. Conversely, a poor starting solution may quickly lead to a poor local minimum after optimization of the design, resulting in a poorer performing product and accruing significant extra cost over an extended production run.

Due to the relative novelty of generalized GRIN technology, few such starting solutions exist for COS. Such lens optimization problems may have a very large number of complex degrees of freedom, accounting for the variation in refractive index coefficients at multiple powers of lens apertures. For more complex optical systems such as wide-angle lenses or telecentric relay lenses, manual construction of a starting solution by manipulation of GRIN coefficients becomes extremely difficult.

Our objective for this work is to devise a method to generate COS starting solutions derived from the optical constructions of homogeneous optical designs. Previous works in the literature have addressed the problem of reconstructing a GRIN lens from a conventional optic. In the field known as *transformation optics*, components such as homogeneous lenses are converted to inhomogeneous (also generally magnetic and anisotropic) media by a coordinate transformation of the lens geometry [4]. The magnetic and anisotropic contributions are often small and disregarded to yield a simpler all-dielectric solution (known as quasi-transformation optics or qTO). While this is a powerful technique, it is difficult to apply to multi-element lens systems, with the boundaries between lens elements leading to discontinuities in the resulting GRIN [5].

Several authors have addressed the inverse problem of refractive index distribution construction via a geometrical optics approach. Nemoto and Makimoto [6] first demonstrated a method to solve for a GRIN distribution given a known ray curve, noting that in such a case, numerous paraxially equivalent index distributions exist for a single ray path. In 2022, Kochan *et al.* [7] demonstrated a method of reconstructing individual

homogeneous surfaces as GRIN media, by use of a sigmoid function GRIN distribution. In 2023, Gomez-Correa *et al.* [8] demonstrated a means to solve for the GRIN distribution given a finite ray path, exploiting an invariant quantity that arises when Fermat's principle is solved via a Lagrangian approach. This invariant quantity was shown to enable analytical solutions to ray paths within spherical and cylindrical gradient-index media.

In the present work, we outline a simple and deterministic method for the conversion of the first-order properties of entire multi-element homogeneous lens systems to COS. This is achieved first by approximating the segmented ray paths of homogeneous lens systems as a smooth, curved ray trajectory, followed by solving for the required GRIN distribution using the Lagrange invariant of the system and ray paths of two paraxial rays that are non-degenerate in field and aperture. The paraxially reconstructed GRIN optic can then serve as a starting point for subsequent finite ray optimization.

2. PARAXIAL RAYTRACING IN GRIN LENSES

The paraxial approximation assumes rays in an optical system travel along a narrow, thread-like region about the optical axis [9,10], which simplifies finite raytracing to a linear form. This approximation trades raytrace precision for insight into the first-order properties of the optic, and following further calculation, the third-order aberrations.

We define a paraxial optical system in Fig. 1. The quantity y represents the height of a paraxial ray. u represents the paraxial ray angle in the anti-clockwise trigonometric convention such that $u \approx \dot{y}$, where dotted quantities represent differentiation with respect to the optical axis coordinate, z. The optical system itself is represented by the green box labelled *ABCD*. Barred quantities are those associated with the paraxially traced full-field principal ray, whereas unbarred quantities are of the paraxial marginal ray. The subscripts O and I represent quantities in the object and image spaces, respectively.

The linearization of raytracing in the paraxial region allows us to represent the optical system as a 2×2 matrix that relates the height and angle of a paraxial ray in the object space to the image space. We represent the optical system of Fig. 1 in this way, treating the object and image space conjugate distances, z_O and z_I, separately:

$$\begin{pmatrix} y_I \\ N_I u_I \end{pmatrix} = \begin{pmatrix} 1 & z_i/N_i \\ 0 & 1 \end{pmatrix} \begin{pmatrix} A & B \\ C & D \end{pmatrix} \begin{pmatrix} 1 & z_O/N_O \\ 0 & 1 \end{pmatrix} \begin{pmatrix} y_O \\ N_O u_O \end{pmatrix}, \tag{1}$$

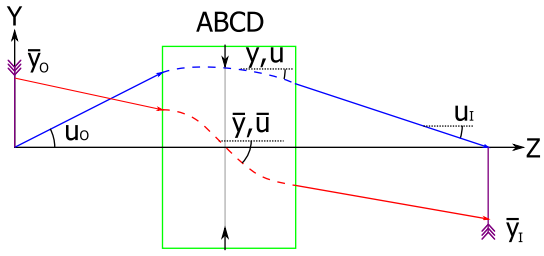

Fig. 1. Schematic of a paraxial COS, *ABCD*. Rays traced are indicated in blue (marginal ray) and red (principal ray). Barred quantities refer to the principal ray.

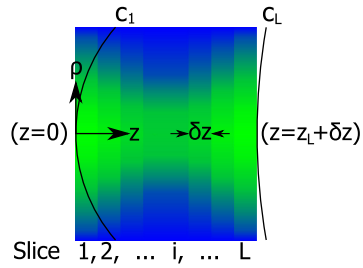

Fig. 2. General rotationally symmetric GRIN decomposed into planar, thin, elemental GRINs of thickness δz. The subscript, L, denotes the last surface of the GRIN.

where the quantities A, B, C, D fully characterize the first-order properties of the system. In particular, the quantity $-C$ is equivalent to the focal power (the inverse of the focal length). The *ABCD* matrix consists of contributions from individual surfaces and ray transfer events between surfaces, representing the system as a product of elemental matrices.

We define a general rotationally symmetric GRIN distribution as a series in even powers of the perpendicular distance from the optical axis, $\rho^2 = x^2 + y^2$, as

$$N(\rho, z) = \mathcal{N}_0(z) + \mathcal{N}_2(z)\rho^2 + \mathcal{N}_4(z)\rho^4 + \dots, \tag{2}$$

where each radial index coefficient, $\mathcal{N}_i$ (distinguished from the refractive index itself by use of the caligraphic $\mathcal{N}$), is a function of position along the optical axis, z (constant coefficients would represent a radial GRIN distribution). The equation of propagation for a GRIN paraxial ray within a distribution of general rotationally symmetric form is given by

$$2\mathcal{N}_2(z)y(z) - \frac{d}{dz}\left(\mathcal{N}_0(z)u(z)\right) = 0. \tag{3}$$

In the general rotationally symmetric case, the transfer matrix of a GRIN has no analytical solution [11]. The paraxial raytrace of the GRIN was therefore performed by slicing the COS into L thin slices, as illustrated in Fig. 2. Following the derivation of Sands [11] the ray path in a thin GRIN slice is then evaluated locally about a point, z, based on a Taylor series expansion of the $\mathcal{N}_0$ and $\mathcal{N}_2$ coefficients:

$$\mathcal{N}_0(z+\delta_z) = \mathcal{N}_0(z) + \dot{\mathcal{N}}_0(z)\delta z + \frac{1}{2}\ddot{\mathcal{N}}_0(z)\delta z^2 + \dots$$

$$\mathcal{N}_2(z+\delta_z) = \mathcal{N}_2(z) + \dot{\mathcal{N}}_2(z)\delta z + \frac{1}{2}\ddot{\mathcal{N}}_2(z)\delta z^2 + \dots \tag{4}$$

where δz is the small, finite thickness along the optical axis of an elemental GRIN located at z. We also expand the ray vector components, $\mathcal{N}_0(z)u(z)$ and $y(z)$, as a series:

$$y(z+\delta z) = y(z) + u(z)\delta z + \frac{\dot{u}(z)}{2}\delta z^2 + \ldots,$$

$$\mathcal{N}_0(z+\delta z)u(z+\delta z) = \mathcal{N}_0(z)u(z) + \frac{d}{dz}\left[\mathcal{N}_0(z)u(z)\right]\delta z + \frac{1}{2}\frac{d^2}{dz^2}\left[\mathcal{N}_0(z)u(z)\right]\delta z^2 + \ldots. \tag{5}$$

The solution to the thin ray transfer matrix has the general form for the ith slice within the GRIN located at z_i:

$$y_{i+1}(z_i+\delta z) = A_i y_i(z_i) + B_i \mathcal{N}_0(z_i)\, u_i(z_i)$$

$$\mathcal{N}_0(z_i+\delta z)\, u_{i+1}(z_i+\delta z) = C_i y_i(z_i) + D_i \mathcal{N}_0(z_i)\, u_i(z_i) \tag{6}$$

To express the equation for the ray trajectory in terms of $y(z)$ and $\mathcal{N}_0(z)u(z)$, we collect expressions for $\dot{u}$, $d/dz[\mathcal{N}_0(z)u(z)]$, and $d^2/dz^2[\mathcal{N}_0(z)u(z)]$, which we substitute into Eq. (5). Expanding Eq. (3) yields

$$2\mathcal{N}_2(z)y(z) - \dot{u}(z)\mathcal{N}_0(z) - \dot{\mathcal{N}}_0(z)u(z) = 0, \tag{7}$$

which solved for $\dot{u}$ is

$$\dot{u}(z) = [2\mathcal{N}_2(z)y(z) - \dot{\mathcal{N}}_0(z)u(z)]\mathcal{N}_0(z). \tag{8}$$

Substituting Eqs. (8) and (3) into Eq. (5), we obtain

$$y(z+\delta z) = y(z) + u(z)\delta z + \frac{\mathcal{N}_2(z)y(z) - \frac{1}{2}\dot{\mathcal{N}}_0(z)u(z)}{\mathcal{N}_0(z)}\delta z^2 + \ldots,$$

$$\mathcal{N}_0(z+\delta z)u(z+\delta z) = \mathcal{N}_0(z)u(z) + 2\mathcal{N}_2(z)y(z)\delta z + \left[\mathcal{N}_2(z)u(z) + \dot{\mathcal{N}}_2(z)y(z)\right]\delta z^2 + \ldots. \tag{9}$$

Collecting terms in $\mathcal{N}_0(z)u(z)$ and $y(z)$ then yields the following equations for A, B, C, D of an elemental GRIN ray-transfer matrix:

$$A_i = 1 + [\mathcal{N}_2(z_i)/\mathcal{N}_0(z_i)]\delta z^2 + \ldots,$$

$$B_i = \delta z/\mathcal{N}_0(z_i) - \frac{1}{2}[\dot{\mathcal{N}}_0(z_i)/\mathcal{N}_0(z_i)^2]\delta z^2 + \ldots,$$

$$C_i = 2\mathcal{N}_2(z_i)\delta z + \dot{\mathcal{N}}_2(z_i)\delta z^2 + \ldots,$$

$$D_i = 1 + [\mathcal{N}_2(z_i)/\mathcal{N}_0(z_i)]\delta z^2 + \ldots. \tag{10}$$

The full system $ABCD$ matrix [as per Eq. (1)] of the COS for a GRIN composed of L slices is given by

$$\begin{pmatrix} A & B \\ C & D \end{pmatrix} = \begin{pmatrix} 1 & 0 \\ c_L\,(N_I - \mathcal{N}_0(z_L)) & 1 \end{pmatrix} \prod_{i=0}^{L} \begin{pmatrix} A_i & B_i \\ C_i & D_i \end{pmatrix} \times \begin{pmatrix} 1 & 0 \\ c_1\,(\mathcal{N}_0(0) - N_O) & 1 \end{pmatrix}. \tag{11}$$

As each internal elemental GRIN is planar (excluding the end surfaces), the surface refraction contribution is the identity matrix and is disregarded. The quantity $-C_i$ gives the focal power of a GRIN ray transfer matrix, yielding the well known formula for the focal power of a thin, radial GRIN lens, $K_{\mathrm{GRIN}} = -2\mathcal{N}_2 t$, for a GRIN of thickness, t. From this, the distribution of $\mathcal{N}_2(z)$ can be intuitively interpreted as the *linear optical power density* of a COS.

The use of a numerical paraxial tracing approach means it is necessary to ensure that enough thin slices are used to avoid numerical errors in ray height and angle. Accuracy of the fit is diagnosed by calculating the determinant of the system $ABCD$ matrix, which should have negligible deviation from unity (in the Nu ray direction convention used). For the lens reconstructions in this work, $L = 2500$ slices, which achieved a determinant error less than 10^{-6} in all cases. We must then perform the paraxial reconstruction by calculating $\mathcal{N}_0(z)$ and $\mathcal{N}_2(z)$ for each GRIN slice within the system.

3. PARAXIAL RECONSTRUCTION

Our approach shall be to identify a GRIN distribution in the form of Eq. (2), such that the ABCD matrix of a homogeneous system is approximated within the same axial length. To achieve a smooth GRIN distribution, we will convert the discrete and segmented trajectory of the paraxial marginal and full-field principal rays within a homogeneous optical system to a smooth ray curve indicative of a GRIN medium describing ray height, y, as a function of the optical axis, z. The process for this we discuss in Sections 4 and 5. An illustrative example of a smoothed ray is shown in Fig. 3. Using these smoothed and fitted rays, we will then solve for the refractive index distribution. To avoid the requirement for a GRIN medium in the object and image space, we bound the GRIN by the first and last surfaces of the homogeneous optic.

Assuming the paraxial ray height, $y(z)$, and its derivatives are known from the reconstruction of the ray, we must devise a procedure to reconstruct the axial and parabolic radial GRIN coefficients, $\mathcal{N}_0(z)$ and $\mathcal{N}_2(z)$, at a point along the optical axis of the lens. To calculate $\mathcal{N}_2(z)$ and $\mathcal{N}_0(z)$ from the smoothed ray paths, we make use of the Lagrange invariant, a conserved quantity of any rotationally symmetric optical system loosely related to energy throughput. The Lagrange invariant is defined as

$$H = \mathcal{N}_0(z)[\bar{u}(z)y(z) - u(z)\bar{y}(z)]. \tag{12}$$

The numerical value of H is obtained from the paraxial rays of the parent homogeneous optical system. This, combined with the reconstructed ray trajectories, gives us sufficient information

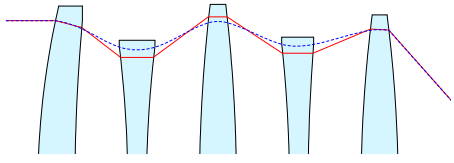

Fig. 3. Notional paraxial ray within a lens system (red line, not to scale) and a reconstructed continuous GRIN trajectory (blue line). Ray positions and angles in both cases are matched at first and last surfaces of the lens system.

to calculate $\mathcal{N}_0(z)$ from Eq. (12). $\dot{\mathcal{N}}_0(z)$ is determined by differentiation of the Lagrange invariant as

$$\dot{\mathcal{N}}_0(z)[\bar{u}(z)y(z) - u(z)\bar{y}(z)) + \mathcal{N}_0(z)\big(\dot{\bar{u}}(z)y(z) - \dot{u}(z)\bar{y}(z)\big] = 0. \tag{13}$$

We then obtain the following expressions for $\mathcal{N}_0(z)$ and $\dot{\mathcal{N}}_0(z)$:

$$\mathcal{N}_0(z) = H/[\bar{u}(z)y(z) - u(z)\bar{y}(z)], \tag{14}$$

$$\dot{\mathcal{N}}_0(z) = [-\mathcal{N}_0(z)^2(\dot{\bar{u}}(z)y(z) - \dot{u}(z)\bar{y}(z))]/H. \tag{15}$$

Once $\mathcal{N}_0(z)$ and $\dot{\mathcal{N}}_0(z)$ are known, we calculate $\mathcal{N}_2(z)$ by solving Eq. (7):

$$\mathcal{N}_2(z) = \frac{1}{2}[\dot{u}(z)\mathcal{N}_0(z) + \dot{\mathcal{N}}_0(z)u(z)]/y(z). \tag{16}$$

4. SELECTION OF A MATHEMATICAL REPRESENTATION FOR RECONSTRUCTED RAY PATHS

A key decision in paraxial reconstruction concerns selection of a tool for the smoothed ray fit. Mathematical constructions were assessed based on three key requirements.

- The fitted curve must match the position and slope of the discrete ray path at the end-points to correctly account for refraction at the end surfaces. This condition ensures that the first-order properties will be accurately reconstructed.
- The curve must be smooth and continuous to at least the second derivative in z to avoid discontinuities in the distribution of $\mathcal{N}_2$.
- The fitted curve should not rely upon least-squares numerical fitting, which adds complexity to the process and does not guarantee a good fit can be found for more complex distributions of refractive index, being vulnerable to over-fitting effects such as the Runge Phenomenon.

Bézier curves were considered ideal candidates based on these criteria. Bézier curves are parametric polynomials in the Bernstein basis [chapter 1.3.4 12] defined by a set of control points (with polynomial order equal to the number of control points minus one). The position and derivative of the curve end-points are defined by the first and last control point segments, fulfilling the first criterion. A set of at least three (non-collinear) control points yields a smooth and continuous curve to the second derivative. Furthermore, Bézier curves do not intersect intermediate control points exactly but approximate them with the property of *diminished variation*. This property minimizes over-fitting effects and the resulting index gradients in the reconstruction.

5. COMPUTATIONAL IMPLEMENTATION

The paraxial reconstruction approach was implemented using the Python programming language. The `bezier` library [13] was used to model the Bézier curves required for ray path smoothing, while elements of the `scipy` ecosystem [14] were used for various other aspects such as spline fitting the resulting index coefficient curves, $\mathcal{N}_0$ and $\mathcal{N}_2$, as a function of the optical axis, z.

Table 1. Basic Parameters for the Parent Double Gauss Lens

F/#	2.0
Focal length	100 mm
Back focal clearance	61.1 mm
Axial length	139 mm
Semi-field of view	14°

An example Double Gauss lens from the CodeV software was used as a homogeneous "parent" lens system. Its basic optical properties are listed in Table 1. A raytrace of this design is shown in Fig. 4A.

Paraxial reconstruction was implemented via the procedure summarized in Fig. 5. The discrete ray paths of the parent optical system were converted to piecewise linearly interpolated functions at a reference wavelength of 587 nm. Sets of evenly spaced control points were defined along each parent ray path that define the Bézier curves. The closeness of the reconstructed ray paths to the parent rays is affected by the number of control points, which for the designs in this work was notionally set to twice the number of optical surfaces of the parent system. Increasing the number of control points results in reconstructed rays that more closely track the parent ray path. This has the effect of increasing the curvature of these rays, which in turn results in a greater magnitude of $\mathcal{N}_2$ and therefore increased index variation in the reconstructed design. The choice of control points is therefore a trade-off between how precisely the paraxial GRIN rays track those of the parent solution, and minimization of index variation in the reconstructed design, which is worthy of investigation in further work. Note that the first-order properties of the design are unaffected by this choice, as the constrained ray slopes and positions at the endpoints of the lens determine this.

Following Bézier fits of the ray paths, these curves and their derivatives with respect to z were input to Eqs. (14) and (16). For computational convenience, a cubic spline fit was made to the reconstructed $\mathcal{N}_0(z)$ and $\mathcal{N}_2(z)$ curves, with control points placed at points along the Bézier curves. Fitting to splines retains

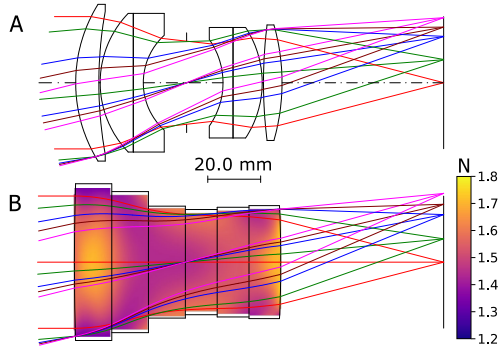

Fig. 4. (A) Raytrace of homogeneous parent Double Gauss lens. Glass types (from the Schott catalogue) from left to right: N-SSK2 ($N_d = 1.622$), N-SK2 ($N_d = 1.607$), F5 ($N_d = 1.603$), F5, N-SK16 ($N_d = 1.620$). (B) Raytrace of optimized COS from paraxially reconstructed starting point.

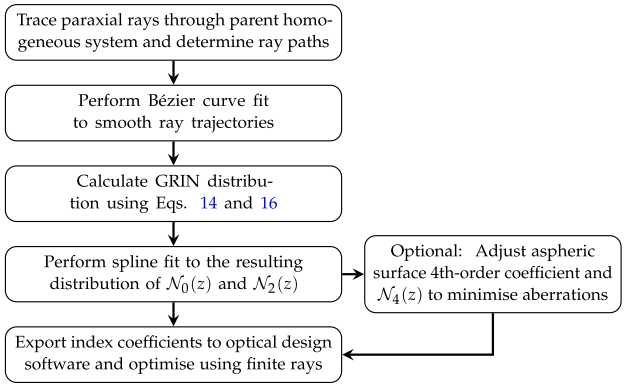

Fig. 5. Flowchart for the paraxial reconstruction process.

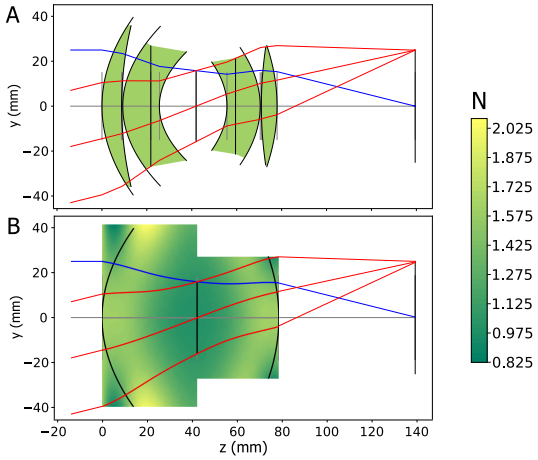

Fig. 6. (A) Paraxial raytrace of parent homogeneous system based on CodeV example F/2 Double Gauss lens. Refractive index of air gaps between lenses is not shaded. (B) Paraxial reconstruction raytrace of the same lens.

the desirable attributes from the shape of the Bézier curves (which would not be obtained by directly fitting to splines), while putting the curves in a mathematical representation that is easier to model and optimize in optical design software.

A further benefit of a spline-distributed GRIN lies in its ability to locally and stably control the axial distribution of GRIN coefficients. For polynomial GRIN distributions of a high degree in the optical axial coordinate, z, it is very difficult to locally control the GRIN distribution at the far end of a thick GRIN lens, relying on the balancing of several polynomial terms, whereas, for a spline GRIN, tactile and local adjustments can be made by changing only a single control point, leading to better conditioning of the finite-ray optimization problem.

A paraxial reconstruction example of the Double Gauss lens is shown in Fig. 6. The Bézier curve fits of the paraxial marginal and principal rays are shown in Fig. 7. From these ray paths, values for $\mathcal{N}_0(z)$ and $\mathcal{N}_2(z)$ were calculated. These distributions are shown in Fig. 8. It is observed that the axial index distribution broadly mirrors that of the parent design, with a noted drop in index aligned with the system air gap. Similarly, the $\mathcal{N}_2(z)$ distribution correlates well with the expected distribution of optical power density (note that linear optical power density is proportional to $-\mathcal{N}_2$). The regions at each end of the system contain positive optical power density, whereas the

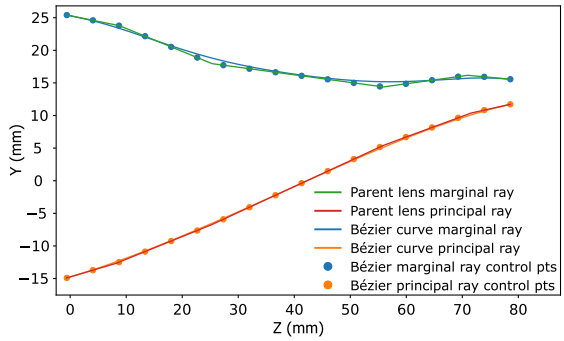

Fig. 7. Homogeneous segmented ray paths, control points, and their Bézier reconstructions for the paraxial marginal and full field principal rays. Double Gauss F/2 example lens.

central region of the paraxial reconstruction around the aperture stop contains negative power density. This leads to the familiar "hourglass" profile of the axial marginal ray we observe in the Double Gauss solution. The focal length of the reconstruction was 99.7 mm, a very close match to the parent design focal length of 100 mm. Spline fits to the reconstructed distributions are also plotted in Fig. 8. A natural cubic spline fit with knots placed at the Chebyshev nodes provides a sufficiently accurate fit to these reconstructed distributions with minimal oscillations.

A. Finite Raytracing and Seidel Aberrations

Paraxial reconstruction does not guarantee the resulting system will have equivalent third-order aberrations to the parent system. The aberrations of a quadratic, radial-GRIN medium are generally different to those of a spherical surface of equivalent optical power. Furthermore, the GRIN distribution generates GRIN surface aberration contributions in addition to the homogeneous surface contributions at the surface vertices [15]. The Seidel aberration contributions of both the homogeneous Double Gauss and COS reconstruction are shown in Fig. 9. It is observed that while the cumulative distribution of the Seidel

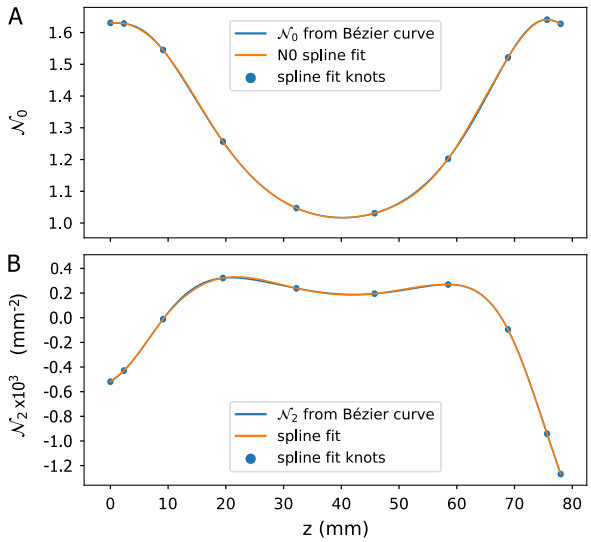

Fig. 8. Reconstructed GRIN coefficients for the Double Gauss design example, with coordinate system origin at the lens front vertex. (A): reconstructed distribution for the axial index, $\mathcal{N}_0(z)$. (B): reconstructed distribution for the quadratic radial coefficient, $\mathcal{N}_2(z)$.

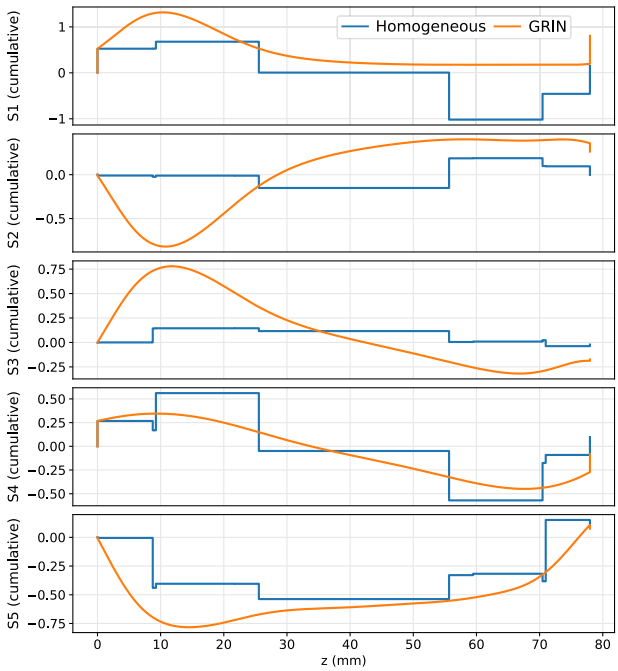

Fig. 9. Cumulative Seidel aberration contributions for the F/2 Double Gauss lens (blue) and its COS paraxial reconstruction (orange). S1–5 represent the Seidel aberration coefficients of spherical aberration, coma, astigmatism, Petzval curvature, and distortion, respectively. The discontinuous changes in cumulative aberration are caused by the discrete Seidel contributions of optical surfaces.

aberrations bears some similarity between the homogeneous and COS starting points, there is ultimately a progressive difference between the two that results in significant Seidel aberration residuals within the GRIN system. Whether this is problematic depends on the aperture, field, and level of aberration. It is sometimes useful to control the Seidel aberrations of the starting point to allow finite raytracing for optimization (such as in very-wide-angle "fisheye" systems that require significant distortion). Reduction of the aberrations can however be achieved more simply by temporarily reducing the field and aperture of the system, restoring them after successive optimizations.

If control of the third-order aberrations is required, then additional degrees of freedom are available to the designer prior to optimization with finite rays. First, aspheric surface terms can be applied to compensate for surface GRIN contributions. Second, the quartic GRIN coefficient, $\mathcal{N}_4(z)$, can be used to control aberrations. Neither of these interventions affects the first-order properties of the reconstructed system.

B. Lens Optimization and Analysis

The resulting paraxially reconstructed starting point was optimized in CodeV using the damped-least-squares "AUT" option to minimize the RMS spot size. The refractive index was constrained to lie between 1.4 and 1.75 within the volume bounded by the rays of the system. These refractive index limits were notional and not indicative of any particular current manufacture technology. The curvature of the rearmost surface was constrained to be convex to preserve back focal clearance (a typical space envelope constraint for photographic lenses).

Table 2. RMS Spot Size over Field for Homogeneous and GRIN Reconstructed-Optimized Double Gauss Solutions

Field (°)	Homogeneous RMS Spot Size (μm)	GRIN RMS Spot Size (μm)
0.0	26.4	7.6
10.0	29.8	11.0
14.0	42.6	17.3

The aspheric terms added to aid initial finite raytracing were optimized to near zero using weighted constraints then removed altogether to leave spherical surfaces in the final design. Back focal distance was kept identical to the homogeneous parent solution. A raytrace cross-section is shown in Fig. 4B with overlaid GRIN distribution.

The RMS spot size (at 587 nm wavelength) of the GRIN solution was smaller than that of the homogeneous lens, which is shown for reference in Table 2; however one must consider with caution that making a direct comparison of performance is not a fair test, as the parent design was corrected for chromatic aberrations, and was presumed to be optimized accordingly, while the GRIN was not.

6. FURTHER WORKED EXAMPLE: LITHOGRAPHIC RELAY LENS

We demonstrate the application of the paraxial reconstruction method to a complex lithographic lens design [16]. Such lens designs feature large numbers of lens elements of modest optical power and produce ray structures that closely resemble the curved ray trajectories of a GRIN. A 14-element stepper lens of NA = 0.2, 589 nm reference wavelength, and 50 mm image diameter at −1 magnification (finite raytrace of the original homogeneous lens shown in Fig. 10A) was paraxially reconstructed as a GRIN. Paraxial traces of the homogeneous parent system and paraxial reconstruction are illustrated in Fig. 11. Distortion and telecentricity of such optical systems are of high importance to the lithographic process. The paraxial reconstruction approach maintains the telecentric entrance and exit pupil locations with a strong degree of fidelity, with both the entrance and exit pupils located over 50 m from the lens vertices. Magnification of the paraxial reconstruction is very similar to the parent design, being −1.0011 and −1.0000, respectively.

The cumulative Seidel aberration contributions of the parent and reconstructed starting system are shown in Fig. 12. Spherical aberration is not corrected by the reconstruction approach but can be corrected in near isolation by changing

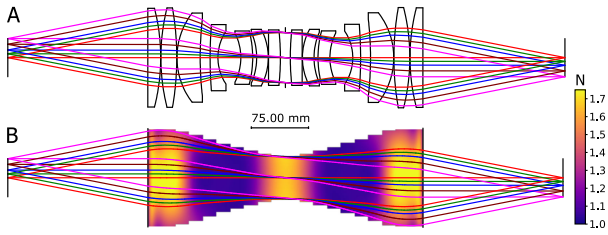

Fig. 10. (A) Finite raytrace of parent homogeneous lithographic lens. (B) Optimized COS solution from paraxially reconstructed starting point, with overlaid GRIN distribution.

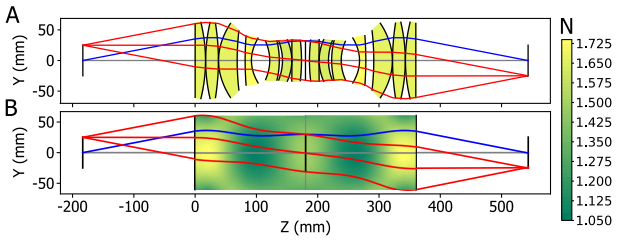

Fig. 11. (A) Paraxial trace of lithographic lens and (B) GRIN paraxial reconstruction.

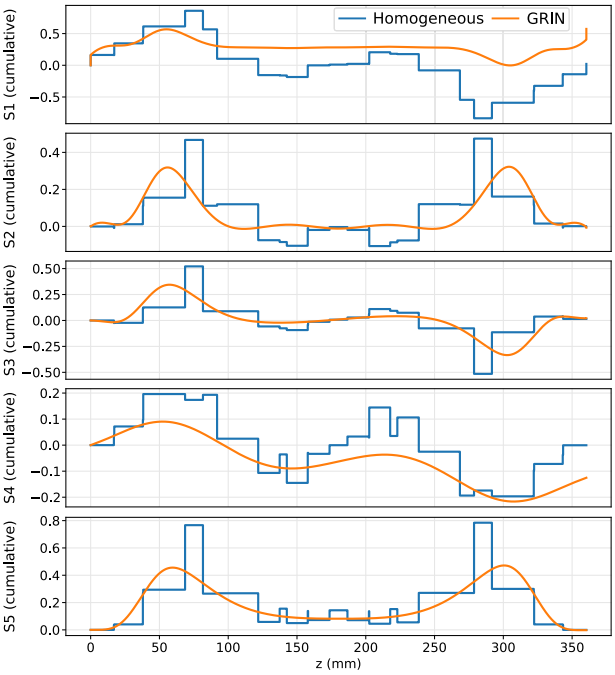

Fig. 12. Cumulative Seidel aberrations of the paraxially reconstructed lithographic lens and homogeneous parent design.

the $\mathcal{N}_4(z)$ coefficient spline knots close to the aperture stop of the system. Coma and distortion are well corrected by the symmetry of the lens. Petzval curvature is observed to gradually diverge from the homogeneous solution, despite a very similar power construction. This is due to a fundamental difference in aberration theory between powered GRIN media and refractive homogeneous lenses [17]. In Eq. (17) we note that for a thin, radial GRIN medium, Petzval curvature depends on power

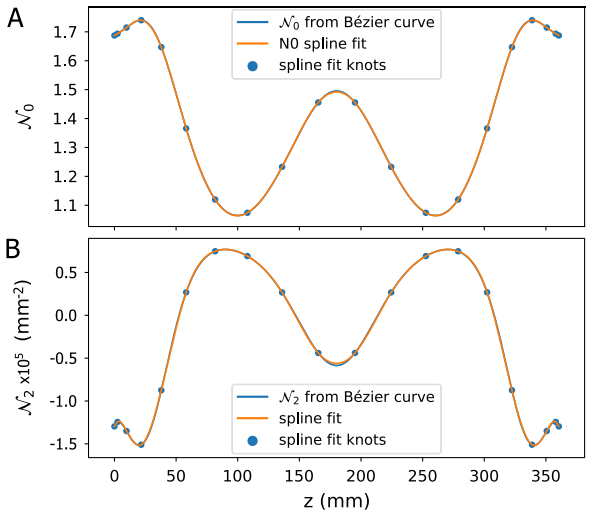

Fig. 13. Lithographic lens paraxial reconstruction outputs. (A) $\mathcal{N}_0$ distribution and associated spline fit. (B) $\mathcal{N}_2$ distribution and associated spline fit.

divided by square of the axial index $\mathcal{N}_0$, whereas for homogeneous lenses the dependency is on optical power divided by the lens refractive index:

$$S4_{\mathrm{GRIN}} = -H^2 \frac{K_{\mathrm{GRIN}}}{\mathcal{N}_0^2},$$

$$S4_{\mathrm{hom}} = -H^2 \frac{K_{\mathrm{lens}}}{N_{\mathrm{lens}}}. \tag{17}$$

The result of this difference in aberration theory is a change in the power construction of the GRIN solution following RMS spot size optimization in CodeV of the paraxially reconstructed starting point. It is observed that the characteristic "central bulge" of the parent lens is absent in the optimized GRIN solution, being replaced by a negatively powered "waist" with a higher axial index. The resulting design is shown in Fig. 10B. The GRIN distribution consisted of 20 spline knots as illustrated in Fig. 13, with individual knots placed at the Chebyshev nodes (this particular distribution of knots being more concentrated at the ends of the GRIN where more structure exists in the distribution). Distortion, telecentricity error (defined as the principal ray incidence angle at the image plane), RMS wavefront error, and RMS spot size are all comparable to the parent solution, as listed in Table 3.

Table 3. Telecentricity, RMS Spot Size, and RMS Wavefront Error with Image Height for the Optimized Paraxially Reconstructed GRIN and Homogeneous Parent Solution

Image Height (mm)	GRIN Telecentrity (°)	Hom. Telecentricity (°)	GRIN RMS Spot Size (μm)	Hom. RMS Spot Size (μm)	GRIN RMS Wavefront Error (Waves at 589 nm)	Hom. RMS Wavefront Error (Waves at 589 nm)	GRIN Distortion (%)	Homogeneous Distortion (%)
0.0	0.0	0.0000	0.271	0.309	0.0063	0.0056	0.0000	0.0000
5.0	0.0799	0.0705	0.306	0.303	0.0066	0.0096	−0.0237	−0.0328
10.0	0.1351	0.1243	0.455	0.939	0.0088	0.0328	−0.0199	−0.0290
17.5	0.1134	0.1347	0.984	1.688	0.0290	0.0780	−0.0089	−0.0180
25.0	0.1271	0.0018	1.819	1.743	0.0450	0.0432	−0.0091	0.0000

7. CHROMATIC PARAXIAL RECONSTRUCTION TO A THREE-MATERIAL GRIN

GRIN lenses are frequently used to correct the chromatic aberrations of optical systems, which motivates us to extend the paraxial reconstruction technique to polychromatic systems. As primary axial and lateral color are caused by the variation of the paraxial properties of an optical system with wavelength, we can accurately reconstruct the color correction of the parent lens, by paraxial reconstruction at three sequential defining wavelengths spanning the operating waveband, $\lambda_{\text{short}} < \lambda_{\text{mid}} < \lambda_{\text{long}}$. With these three paraxial reconstructed systems we define two key quantities, the axial GRIN dispersion $\mathcal{N}_{0\lambda}$ and the distributed GRIN second-order dispersion $\mathcal{N}_{2\lambda}(z)$, defined as

$$\mathcal{N}_{0\lambda}(z) = \mathcal{N}_0(\lambda_{\text{long}}, z) - \mathcal{N}_0(\lambda_{\text{short}}, z),$$
$$\mathcal{N}_{2\lambda}(z) = \mathcal{N}_2(\lambda_{\text{long}}, z) - \mathcal{N}_2(\lambda_{\text{short}}, z). \quad (18)$$

Once these dispersion curves are known, we fit the reconstructed $\mathcal{N}_0(\lambda_{\text{mid}}, z)$, $\mathcal{N}_2(\lambda_{\text{mid}}, z)$, $\mathcal{N}_{0\lambda}(z)$, and $\mathcal{N}_{2\lambda}(z)$ profiles to a basis of constituent materials that form the GRIN starting solution. Fitting a GRIN to a spatial distribution of base materials enables improved design for manufacture, by expressing the GRIN lens in terms of what can be made. For a GRIN consisting of two base materials, the axial and radial GRIN dispersion is constant (with paraxial reconstruction at a single wavelength all that is required). A three-material GRIN is required to fit the base index, $\mathcal{N}_0(z)$, axial dispersion, $\mathcal{N}_{0\lambda}(z)$, index gradient, $\mathcal{N}_2(z)$, and gradient dispersion, $\mathcal{N}_{2\lambda}(z)$, as a function of position.

Previous works [18,19] have outlined mathematical representations for the refractive index of GRIN lenses consisting of three or more materials as a weighted average of the relative composition of the constituent materials. We define the refractive index of a three-base-material GRIN lens as

$$N = \frac{N_A m_A(\rho, z) + N_B m_B(\rho, z) + N_C m_C(\rho, z)}{m_T(\rho, z)}, \quad (19)$$

where $m_T(\rho, z) = m_A(\rho, z) + m_B(\rho, z) + m_C(\rho, z)$. We require the values of $m_A(\rho, z)$, $m_B(\rho, z)$, and $m_C(\rho, z)$, as well as a defined set of base materials, $N_A(\lambda)$, $N_B(\lambda)$, and $N_C(\lambda)$, to fully define the GRIN distribution at a given point. $m(\rho, z)$ for the nth material is given by

$$m_n(\rho, z) = m_{n0}(z) + m_{n2}(z)\rho^2 + m_{n4}(z)\rho^4 + \ldots. \quad (20)$$

We constrain that $m_T(\rho, z) = 1$, which allows us to easily decompose Eq. (19) into contributions from each material, giving

$$m_{A0}(z) + m_{B0}(z) + m_{C0}(z) = 1, \quad (21)$$

$$m_{A2}(z) + m_{B2}(z) + m_{C2}(z) = 0. \quad (22)$$

This then yields refractive index coefficients

$$\mathcal{N}_0(z) = N_A m_{A0}(z) + N_B m_{B0}(z) + N_C m_{C0}(z), \quad (23)$$

$$\mathcal{N}_2(z) = N_A m_{A2}(z) + N_B m_{B2}(z) + N_C m_{C2}(z). \quad (24)$$

Using Eq. (18) yields the GRIN coefficient dispersion

$$\mathcal{N}_{0\lambda}(z) = N_{A\lambda} m_{A0}(z) + N_{B\lambda} m_{B0}(z) + N_{C\lambda} m_{C0}(z), \quad (25)$$

$$\mathcal{N}_{2\lambda}(z) = N_{A\lambda} m_{A2}(z) + N_{B\lambda} m_{B2}(z) + N_{C\lambda} m_{C2}(z), \quad (26)$$

where the dispersion of the nth basis material is given by $N_{n\lambda} = N_n(\lambda_{\text{long}}) - N_n(\lambda_{\text{short}})$. Equations (21)–(26) form a set of six linear equations, while we have six unknowns: $m_{A0}(z)$, $m_{B0}(z)$, $m_{C0}(z)$, $m_{A2}(z)$, $m_{B2}(z)$, and $m_{C2}(z)$. This therefore allows this system of equations to be solved exactly, giving:

$$m_{A0}(z) = [N_B N_{C\lambda} - N_C N_{B\lambda} + \mathcal{N}_0(z)\,(N_{B\lambda} - N_{C\lambda}) - \mathcal{N}_{0\lambda}(z)\,(N_B - N_C)]\,\phi^{-1}, \quad (27)$$

$$m_{B0}(z) = [-N_A N_{C\lambda} + N_C N_{A\lambda} - \mathcal{N}_0(z)\,(N_{A\lambda} - N_{C\lambda}) + \mathcal{N}_{0\lambda}(z)\,(N_A - N_C)]\,\phi^{-1}, \quad (28)$$

$$m_{C0}(z) = [N_A N_{B\lambda} - N_B N_{A\lambda} + \mathcal{N}_0(z)\,(N_{A\lambda} - N_{B\lambda}) - \mathcal{N}_{0\lambda}(z)\,(N_A - N_B)]\,\phi^{-1}, \quad (29)$$

$$m_{A2}(z) = [\mathcal{N}_2(z)\,(N_{B\lambda} - N_{C\lambda}) - \mathcal{N}_{2\lambda}(z)\,(N_B - N_C)]\,\phi^{-1}, \quad (30)$$

$$m_{B2}(z) = [-\mathcal{N}_2(z)\,(N_{A\lambda} - N_{C\lambda}) + \mathcal{N}_{2\lambda}(z)\,(N_A - N_C)]\,\phi^{-1}, \quad (31)$$

$$m_{C2}(z) = [\mathcal{N}_2(z)\,(N_{A\lambda} - N_{B\lambda}) - \mathcal{N}_{2\lambda}(z)\,(N_A - N_B)]\,\phi^{-1}, \quad (32)$$

where $\phi = N_A N_{B\lambda} - N_A N_{C\lambda} - N_B N_{A\lambda} + N_B N_{C\lambda} + N_C N_{A\lambda} - N_C N_{B\lambda}$. Computationally, these coefficients were determined via an analogous method to that outlined for monochromatic paraxial reconstruction. $\mathcal{N}_0(z, \lambda)$ and $\mathcal{N}_2(z, \lambda)$ were calculated via the fitting of Bézier curves to the paraxial rays of the parent optical system at λ_{short}, λ_{mid}, and λ_{long}. The paraxial raytrace at the central reference wavelength was used to define $\mathcal{N}_0(z, \lambda_{\text{mid}})$ and $\mathcal{N}_2(z, \lambda_{\text{mid}})$, while the difference between the short and long wavelength systems was used to define $\mathcal{N}_{0\lambda}(z)$ and $\mathcal{N}_{2\lambda}(z)$. The resulting curves for $\mathcal{N}_0(z)$, $\mathcal{N}_2(z)$, $\mathcal{N}_{0\lambda}(z)$, and $\mathcal{N}_{2\lambda}(z)$ were then input to Eq. (27)–(32) to yield curves defining the relative composition coefficients of the lens. Spline knots were then fitted to these curves, with these knots being the outputs of the code that was input to a spline-based, three-material GRIN dynamic-link-library (DLL) to raytrace the system in CodeV. Three materials and their associated properties were defined as input parameters for the reconstruction. In principle, any three unique materials (with non-identical index and dispersion) can be used to fit relative composition; however the index and dispersion space defined by materials A, B, and C should be comparable to that defined by the materials of the parent system. If the range of index and dispersion values differs significantly between the parent lens and GRIN reconstruction, then significant regions of unphysical negative composition may exist in the paraxial reconstruction. While such regions are generally simple to address through

Table 4. Optical Specification for the Cooke Triplet Parent Lens Design

Focal length	50.00 mm
F/#	5.0
Field of view	40°
Wavelengths	486.1, 546.1, 656.3 nm
Spectral weight	1, 2, 1
Glass types	N-SK16, N-F2, N-SK16
Back focal clearance	38.71 mm
Overall length	57.55 mm

optimization, correction of excessive material errors can lead to poor local minima in the optimized design.

A Cooke triplet example lens system (sample lens provided with CodeV) was reconstructed over a finite waveband. The specification of this lens is listed in Table 4. For consistency, the GRIN basis materials A, B, and C were equivalent to the parent system (N-SK16, N-F2, and air). While this design is not indicative of any current GRIN manufacture approach, it is used to demonstrate the technique and the first-order equivalence of the reconstructed solution.

The relative composition of the paraxially reconstructed GRIN starting point is shown in Fig. 14. Notably, there are significant regions of negative composition in N-F2 (material B), with a corresponding excess of N-SK16 (material A). This is due to the very similar refractive index between these two materials. Such material space errors are corrected through the imposition of constraints during finite-ray optimization. The similar index of these materials allows restoration of all positive $m_n(\rho, z)$ values within the lens without significant disturbance to the optimization that may cause descent into a poor local minimum.

The paraxially converted starting point is shown alongside a paraxial trace of the parent solution in Fig. 15. The focal length of the converted system matches the parent solution closely, at 49.62 mm compared to 50.00 mm. The focal length versus wavelength of the paraxial reconstruction and parent design is shown in Fig. 16. It was observed that the chromatic aberration closely replicates that of the parent solution, being offset by

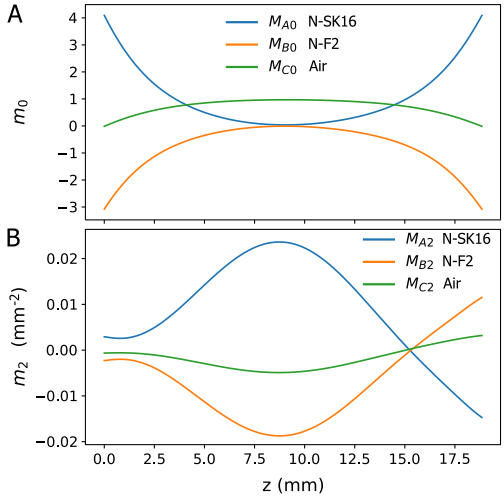

Fig. 14. Reconstructed relative composition distribution of Cooke triplet parent design. (A) Axial relative composition m_0 versus z. (B) Second-order m_2 distribution for each constituent material.

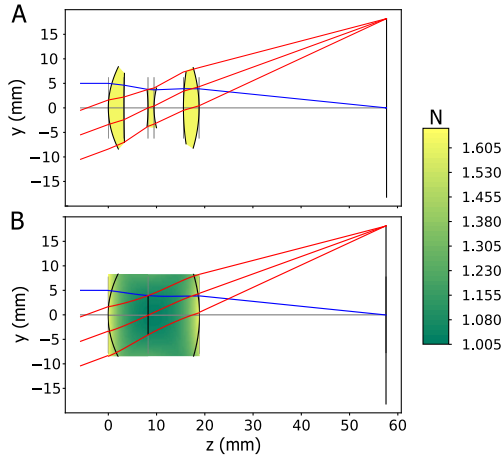

Fig. 15. (A) Conventional Cooke triplet paraxial raytrace. (B) Paraxially reconstructed GRIN paraxial raytrace.

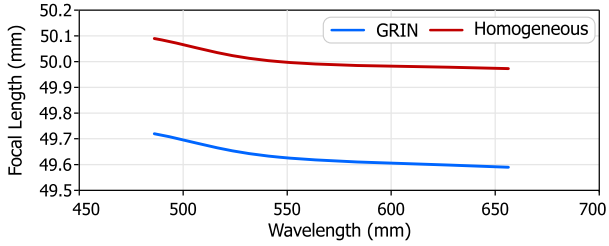

Fig. 16. Focal length versus wavelength of the paraxial reconstructed GRIN Cooke triplet lens and its homogeneous parent.

an approximately constant amount as a result of the ray path smoothing.

Following optimization in CodeV, the GRIN system and homogeneous parent lens are shown in Fig. 17. Optical performance of the GRIN solution is significantly better than the homogeneous starting solution (listed in Table 5); however we note that the GRIN design has more degrees of freedom than the homogeneous solution and is not based on any current GRIN technology. Rather, this solution is intended to demonstrate the utility of the paraxial reconstruction technique, yielding a GRIN analogue to a homogeneous design. The relative composition of the optimized GRIN solution is shown in Fig. 18. The distribution of material within this lens is analogous to the homogeneous parent solution, with a higher concentration of N-SK16 close to the two refractive surfaces at each end of the lens, and a negatively powered central region. One notable difference is the shift of concentration of N-F2 from the center of the lens to the lens surfaces. The large central region of the

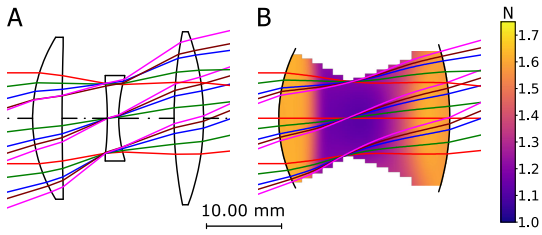

Fig. 17. (A) Conventional Cooke triplet design. (B) Converted and optimized COS design.

Table 5. Polychromatic RMS Spot Size of Cooke Triplet Homogeneous Parent Lens and Optimized GRIN Solution from Paraxially Reconstructed Starting Point

	RMS Spot Size, Table 4 Waveband (μm)	
Field Angle (°)	Homogeneous Parent	GRIN Optimized
0.0	10.2	6.8
7.0	14.9	5.6
14.0	34.3	8.3
17.0	35.9	10.5
20.0	22.6	13.8

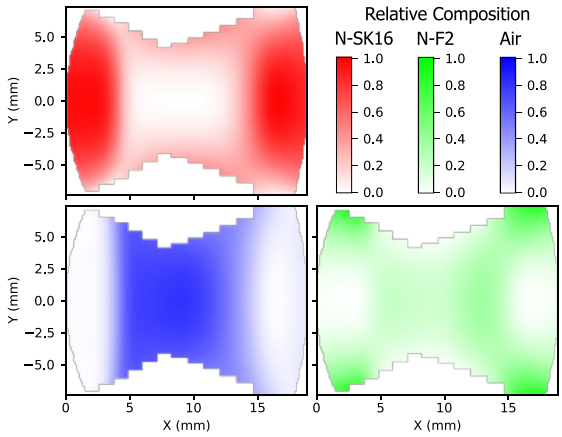

Fig. 18. Relative composition of optimized COS reconstructed from the Cooke triplet.

lens dominated by air indicates that should a smaller ΔN GRIN combination be required for manufacturing feasibility, the solution may function well as two lenses separated by an air gap containing the aperture stop.

8. CONCLUSIONS

The optical design of generalized GRIN continuous optical systems (COS) is a significant optical design challenge, due to a very large parameter space and computationally intensive raytracing. We have demonstrated a method to simplify the optimization approach by starting point generation, based on the choice of COS that share equivalent paraxial properties to homogeneous lenses. This was achieved by smoothing of the discrete, segmented paraxial ray paths of homogeneous systems to target paraxial GRIN ray trajectories, followed by calculation of the requisite GRIN properties using a paraxial raytracing equation for GRIN media and the Lagrange invariant; a technique we refer to as paraxial reconstruction. These converted designs successfully replicate the first-order optical properties of the parent design with strong fidelity.

We have demonstrated several paraxial reconstructions of common lens system types, yielding COS with comparable optical performance to their homogeneous parent solutions following finite-ray optimization. Furthermore, we have demonstrated that the technique is extensible to finite waveband systems through reconstruction at multiple wavelengths.

With the present technique, the Seidel aberrations of the parent system are not converted; however lens design principles such as bilateral symmetry of rays about the aperture stop apply for GRIN media, yielding starting points corrected for aberrations such as coma, lateral color, and distortion. Aberrations of the COS solution can be further addressed through manipulation of the fourth-order $\mathcal{N}_4(z)$ coefficient and through aspheric end surfaces without affecting the first-order properties, or quite simply by optimization of a finite ray model. Promisingly, if this technique is augmented by a fitting approach for a finite marginal ray on axis, in a manner similar to those outlined in [6,8], then a deterministic procedure for a starting solution corrected for spherical aberration and coma is possible (by constraining the image plane ray to fulfill the Abbé sine condition). With continuing development, paraxial reconstruction may serve as the foundation of a powerful suite of techniques to simplify generalized GRIN design and optimization problems.

Acknowledgment. The support provided by Excelitas St Asaph in the preparation of this work is gratefully acknowledged.

Disclosures. The authors declare no conflicts of interest.

Data availability. The lens design prescriptions in this work are available upon reasonable request.

REFERENCES

1. D. Conkey, G. Williams, C. Dupuy, *et al.*, "Additively manufactured freeform gradient-index optics," Proc. SPIE **11889**, 118890R (2018).
2. R. Dylla-Spears, T. D. Yee, K. Sasan, *et al.*, "3D printed gradient index glass optics," Sci. Adv. **6**, eabc7429 (2020).
3. C. Ocier, C. Richards, D. Bacon-Brown, *et al.*, "Direct laser writing of volumetric gradient index lenses and waveguides," Light Sci. Appl. **9**, 196 (2020).
4. J. Li and J. Pendry, "Hiding under the carpet: a new strategy for cloaking," Phys. Rev. Lett. **101**, 203901 (2008).
5. S. D. Campbell, J. Nagar, and D. H. Werner, "Multi-element, multi-frequency lens transformations enabled by optical wavefront matching," Opt. Express **25**, 17258–17270 (2017).
6. S. Nemoto and T. Makimoto, "Refractive-index distribution for a prescribed ray path," J. Opt. Soc. Am. **69**, 450–454 (1979).
7. N. S. Kochan, G. R. Schmidt, and D. T. Moore, "Replacing optical surfaces with gradient index functions which preserve ray trajectory," Opt. Lett. **47**, 1311–1314 (2022).
8. J. E. Gómez-Correa, A. L. Padilla-Ortiz, J. P. Trevino, *et al.*, "Symmetric gradient-index media reconstruction," Opt. Express **31**, 29196–29212 (2023).
9. H. Hopkins, "The nature of the paraxial approximation I. Systems of uniform refractive index," J. Mod. Opt. **38**, 427–445 (1991).
10. H. Hopkins, "The nature of the paraxial approximation II. Systems containing media of radial and of axial non-uniform refractive index: invariants," J. Mod. Opt. **38**, 447–472 (1991).
11. P. J. Sands, "Inhomogeneous lenses, III. Paraxial optics," J. Opt. Soc. Am. **61**, 879–885 (1971).
12. N. Patrikalakis and T. Maekawa, *Shape Interrogation for Computer Aided Design and Manufacturing* (Springer, 2002).
13. D. Hermes, "Helper for Bézier curves, triangles, and higher order objects," J. Open Source Softw. **2**, 267 (2017).
14. P. Virtanen, R. Gommers, T. E. Oliphant, *et al.*, "SciPy 1.0: fundamental algorithms for scientific computing in Python," Nat. Methods **17**, 261–272 (2020).
15. P. J. Sands, "Third-order aberrations of inhomogeneous lenses," J. Opt. Soc. Am. **60**, 1436–1443 (1970).
16. The high resolution projection copying magnification lens, JP,47-035017,B(1972), 1972, https://www.j-platpat.inpit.go.jp/c1801/PU/JP-0681382/15/en.
17. F. Bociort and J. Kross, "Seidel aberration coefficients for radial gradient-index lenses," J. Opt. Soc. Am. A **11**, 2647–2656 (1994).
18. A. M. Boyd, "Optical design of multi-material, general rotationally symmetric GRIN lenses," Proc. SPIE **10998**, 109980J (2019).
19. J. N. Mait, G. Beadie, R. A. Flynn, *et al.*, "Dispersion design in gradient index elements using ternary blends," Opt. Express **24**, 29295–29301 (2016).